Investigation of a Critical Separation Criterion for Mode I-Governed Fracture of Basalt Fiber/Polypropylene Rods via a Modified Double Cantilever Beam Test

Yuta Tobata[a]*, Kimiyoshi Naito[a,b] and Jonathon Tanks[a]

[a] *Research Center for Structural Materials, Polymer Matrix Hybrid Composite Materials Group, National Institute for Materials Science (NIMS), 1-2-1 Sengen, Tsukuba, Ibaraki 305-0047, Japan*

[b] *Tohoku University*

Department of Aerospace Engineering 6-6-01, Aramaki Aza Aoba, Aoba-ku, Sendai, Miyagi, 980-8579, Japan

Email: TOBATA.Yuta@nims.go.jp and yuta.tobata@community.isunet.edu

Abstract

A new approach using a modified double cantilever beam test was proposed for evaluating the mode I-governed critical energy release rate representative of unidirectional composite rods, defined here as the mode I critical separation energy, SE_{IC}. This approach was used to characterize basalt fiber reinforced polypropylene rods. The relation between load and displacement is obtained from loading-holding-unloading tests, where apparent crack length—defined as the straight-line distance between the loading axis and crack tip—is measured at the end of holding time of each cycle; the start of crack propagation is confirmed by in-situ digital microscope observation. Scanning electron microscope observation of fracture surface reveals matrix crack growth and fiber-matrix interfacial debonding. The linear relation between apparent crack length and cube root of compliance is obtained, and the SE_{IC} calculated by the compliance method is 1.5 ± 0.5 kJ/m^2.

Key word

DCB, FRP rod, separation energy, basalt fiber, polypropylene

1. Introduction

Fiber reinforced polymer (FRP) composites have been used for the infrastructures such as bridge decks, offshore wind turbine platforms, and oil and gas field structures as an alternative to steel because of its superior specific tensile strength and modulus [1-3]. One of candidates for reinforcement fibers is basalt fiber (BF). BF has higher tensile strength and modulus than glass fiber [4,5], as well as superior corrosion resistance—particularly in saline and acid environments. The financial cost is reasonable comparing to that of carbon fibers [4,5]. Polypropylene (PP) is a good matrix material candidate for FRP for building construction applications, given it has tensile properties comparable to epoxy resin and is extremely moisture-resistant [6-8].

BF reinforced PP matrix composites (BFPP) may have potential for replacing glass FRP composites where weight and durability are a concern. Previous studies of BFPP laminates report their mechanical properties, investigating the tensile [9-12] and flexural [10] behavior. Weak interfacial strength between BF and PP was revealed by the droplet test [10]. The single edge notch tensile test (SENT) and Izod impact test of BFPP laminates were also conducted to measure the mode I fracture toughness K_{IC} for verifying the reinforcing performance by changing BF content [9-11,13-15].

Meanwhile, in addition to these mechanical properties, the mode I critical energy release rate G_{IC} is also an important parameter for understanding the fracture criterion and mechanics of FRP. One valid method for measuring G_{IC} is the double cantilever beam (DCB) test, such as that

prescribed by ASTM D5528. The test was standardized and improved for many kinds of FRP laminates including BFPP under static and fatigue load conditions [16-20]. This property is useful for predicting the fracture of damaged materials by measuring crack length. In addition, it enables the prediction of stress-strain or load-displacement relations accurately by using a cohesive zone method in finite element analysis [21-25].

Regarding the directional rod geometry of BFPP for buildings and construction, however, there are no reports of G_{IC} calculation approaches. In order to predict the strength and fracture of the rod-shaped composite, it is therefore necessary to determine the G_{IC} of rods as well as laminates. It would be ideal to conduct DCB tests with a rectangular cross-section for predicting the strength and fracture of BFPP rod more precisely. However, the geometric characteristics of a cylindrical rod must be analyzed to be representative of the material used in real structures. This study aims to measure a representative value of the mode I-governed critical fracture energy of BFPP rods by using the DCB test, which has been modified for analyzing cylindrical unidirectional FRP specimens.

2. Experimental Method

2.1. Material

BFPP rods were fabricated at the Kanazawa Institute of Technology, using heat-resistant basalt fibers (Nakagawa Sangyo, Co., Ltd., Japan) having an average diameter of 19 μm, and maleic

anhydride-compatibilized PP (Prime Polymer, Co., Ltd., Japan; Mitsui Chemicals, Co., Ltd., Japan). Figure 1(a) shows the outer surface of the BFPP rods, where the fibers are aligned in the longitudinal direction. Cross sectional images of the rod (Figure 1(b) and (c)) reveal a 0.4 mm-thick PP layer around the 4.4 mm-diameter rod. The fiber volume content calculated from the cross section was 44 %.

2.2. Testing method

The Young's modulus was measured by tensile tests using a universal testing machine (AGX-V, SHIMADZU Co., Ltd., Japan). The BFPP rod was cut to 250 mm lengths and two steel pipes were attached to both ends using an expansive demolition agent (BRISTAR, Taiheiyo Materials Corporation Co., Ltd., Japan). Longitudinal strain was measured by a video extensometer system (TRViewX, SHIMADZU Co., Ltd., Japan). The Young's modulus was calculated as 27±1 GPa by measuring the slope of linear section of stress-strain curve after testing two specimens.

Rod DCB specimens were prepared as shown in Figure 2. Specimens were first cut to the appropriate length with steel circular saw. Notches were cut with a thin diamond circular saw (0.1 mm thickness). Finally, the specimen was separated with a razor blade (0.38 mm thickness). The cantilever sections of each specimen were bent by hand. Eleven samples were prepared.

Rod DCB tests were performed on a tensile testing machine (EZ-S, SHIMADZU Co., Ltd., Japan) under crosshead displacement control, as shown in Figure 3. Specimens were sandwiched

with sandpaper and fixed in the DCB gripping jig. A digital microscope (VHX-6000, KEYENCE Co., Ltd., Japan) was attached to the testing machine for in-situ observation of deformation behavior and measurement of apparent crack length. The crack length was measured as the straight-line distance between the loading axis and crack tip. Preloading was conducted until the load change stopped for making a naturally shaped crack from an artificial crack, after which the load was removed. The rod DCB specimen was attached on the tensile jig and pulled upwards at a crosshead speed of 1.0 mm/min until a stable crack formed. The linear relation between load P and displacement U was found at the beginning of loading and the compliance C ($=U/P$) was estimated. Once stable crack growth was distinguished, the crosshead was stopped and held. When the crosshead was held, the crack gradually grew while the load decreased. The apparent crack length was measured when the load change was stopped. After the crack length measurement, specimens were unloaded. Unloading was stopped when the load was reached 5 N. Similar loading-holding-unloading procedures were repeated up to final separation of the specimen. After testing, fractured surfaces of specimens were observed using scanning electron microscope (SEM) (Quanta 200 F, FEI Company, USA).

3. Results and discussions

3.1. Loading-displacement curve and deformation behavior

Figure 4 represents a typical example of the load-displacement relation and deformation behavior of rod DCB tests. A nearly linear load-displacement relation was observed until the load reached point B, whereas crack propagation was not found (A-B section). Then, the load nonlinearly increased with increasing displacement (B-C section). Figure 4(a) and 4(b) show the comparison of typical deformation behavior between B and C. X_1 stands for the crack tip at B and X_2 is the crack tip at C. Crack growth and large deformation were confirmed. Fiber bridging was also found as indicated by the arrow in Figure 4(b). After the load reached the maximum load (hereinafter referred to as P_{max}), the load decreased with increased displacement, whereas the crack gradually grew up (C-D section). During the crosshead hold (D-E section), the load radically dropped. Meanwhile, the crack opened and propagated. Hereinafter, we defined the load at the end of crosshead hold as P_{arrst}. In the end of cross head hold, apparent crack length was measured. After the measurement, specimens were unloaded. In unloading, the nonlinear load-displacement relation was found until the load reached 5 N (E-F section).

In the F-G section, the graph shows almost linear load-displacement relation again. Crack propagation was not confirmed as well. When the load reached P_{arrst}, the load-displacement relation started to show nonlinear tendency. Figure 4(c) and 4(d) compares the typical deformation behaviours observed before and after P_{arrst} is reached. Y_1 and Y_2 denotes the crack tip before and after reaching P_{arrst}, respectively. The images show slight crack opening and propagation. This indicates that the beginning of the nonlinear loading-displacement region is a result of crack growth.

Above the P_{arrst}, the load-displacement relation and crack propagation behavior (G-I section) shows the same tendency as those of the previous cycles up to the final separation.

3.2. Relation between crack length and cube root of compliance

Figure 5 presents the relationship between apparent crack length and cube root of compliance. A linear relation between them was observed, which can be described by the following equation:

$$C^{1/3} = A_1 a + A_0 \quad (1)$$

where A_1 and A_0 are experimental constants. Compliance can be also calculated by assuming the semi-cylinder shape and isotropy of beams for simplification:

$$C^{1/3} = \sqrt[3]{\frac{2}{3E_L I}}\, a + \sqrt[3]{\frac{2}{3E_L I}}\, xd \quad (2)$$

$$I = \frac{d^4(9\pi^2 - 64)}{1152\pi} \quad (3)$$

where d is diameter of rod, E_L denotes longitudinal Young's modulus, x is modified coefficient considering edge effects. For simplification, we substitute 0.68 assuming isotropy [17];

The relation between crack length and estimated compliance is shown in the Figure 5. It is found that the inclination is parallel to the results. This suggests that the estimation of coefficient A_1 is predictable from elastic beam theory; however, A_0 did not fit the estimation. This seems to derive from the effect of anisotropy on x. Equations proposed by Williams [17] indicate that x predominantly depends on the ratio of Young's modulus and shear modulus. However, in the current study, accurate measurement of the shear modulus was deemed unfeasible due to the geometry of the

rod, so isotropy was assumed. If we fit the estimated A_0 to that of the experimental result as shown in Figure 5, x and shear modulus G were found 2.7-5.9 and 0.21-1.2 GPa, respectively. The predicted shear modulus is within an order of magnitude to that of unidirectional glass fiber reinforced vinyl ester matrix composite (1.3 GPa [26]). The shear modulus of the rod seems predictable by using the proposed rod DCB test. However, further experiments and analysis are required to verify this. Hereafter, we calculate the critical fracture energy by referring the experimental relation between apparent crack length and cube root of compliance.

3.3. Evaluation of mode I-governed separation energy SE_{IC}

Referring to images of deformation in Figure 4, it is clear that the specimen largely deformed. This result suggests that the measured critical energy release rate of this study is different from that measured by the conventional DCB test. Therefore, we define a representative energy release rate called the mode I-governed separation energy, SE_I. If the specimen did not deform largely as shown in the Figure 4(a) and (b), SE_I would be identical to the energy release rate G_I..

Mode I-governed separation energy SE_I can be calculated from the following equation;

$$SE_I = \frac{P^2}{2D} \cdot \frac{dC}{da} \tag{4}$$

Substituting Eq. (1) to Eq. (4) yields

$$SE_I = \frac{P^2}{2D}\left(3{A_1}^3 a^2 + 6{A_1}^2 A_0 a + 3A_1{A_0}^2\right) \tag{5}$$

where P denotes load. As observed in Figure 4(b) and (c), cracks started propagating when the load reaches the identical value to P_{arrst} in each last cycle. On the other hand, specimens largely deformed before P_{max} loaded. This suggests that P_{max} is not proper for evaluation of the critical energy release rate. Therefore, we substituted P_{arrst} into (Eq. 5) for the calculation of the critical separation energy.

$$SE_{IC} = \frac{{P_{arrst}}^2}{2D}\left(3{A_1}^3a^2 + 6{A_1}^2A_0a + 3A_1{A_0}^2\right) \quad (6)$$

Figure 6 shows a relation between $SE_{IC}$and crack length. The SE_{IC} showed 1.5 ± 0.5 kJ/m^2 independently of the apparent crack length.

3.4 SE_{IC} of rod composite vs G_{IC} of matrix

In this section, we measured the fracture toughness of the neat PP matrix material for comparing to that of BFPP by SENT and SENB tests (SENT, 2 replicates; SENB, 3 replicates) following the method of previous reports [27,28]. Dog-bone shape specimens (Figure 7) were fabricated with an injection molding machine (HAAKE MiniJet Pro, Thermo Fisher Scientific Co., Ltd., USA). Notches were cut to 1.5 -1.8 mm lengths. We calculated the critical energy release rate G_{IC} considering the thin geometry and in-plane stress condition of specimen, referring to the literature for Poison's ratio of PP (ν = 0.43) [29].

Table 1 shows a summary of substitutions, G_{IC} of neat PP and SE_{IC} of BFPP. G_{IC} was 1.4 (± 0.3) kJ/m^2 and 1.1 (± 0.2) kJ/m^2 measured by SENT and SENB, respectively. Both of them are close

to SE_{IC} of BFPP. Therefore, it seems that the matrix fracture is a dominant factor for the overall fracture behavior of the BFPP rod.

3.5 Relation between fracture behavior and SE_{IC}

To identify the reason for close agreement between SE_{IC} of the rod composite and G_{IC} of the matrix PP, we first observed the fracture surfaces by SEM (Figure 8(a)). There was little PP attached to the fibers, which were mostly intact. Similar behaviour was also observed from reports of BFPP laminates [10,30]. This suggests that weak fiber-matrix interface adhesion strength caused BF-PP interfacial debonding. Figure 8(b) shows the fracture surface of a matrix region. Elliptical hackles accompanying crack growth are indicated with arrows. The fracture behavior is similar to that of the DCB test of polycarbonate and polystyrene sandwich materials [31].

These findings imply that three components of G_{IC} (matrix, fiber, matrix-fiber interface) are related to the SE_{IC} of the rod. Provided the total crack length of each area with the relation

$$a_{total} = a_m + a_f + a_i \tag{7}$$

where a_{m}, a_{f} and a_{i} are the crack lengths of the matrix, fiber and fiber-matrix interface respectively, and the strain energy relation between that of each area is

$$U_{total} = U_m + U_f + U_i \tag{8}$$

the equation of energy release rate under constant load

$$G_{\mathrm{IC}} = \frac{1}{B}\left(\frac{dU}{da}\right) \tag{9}$$

can be transformed into

$$SE_{\mathrm{IC}} = \frac{1}{B}\left(\frac{dU}{da_{total}}\right) = \frac{1}{B}\left(\frac{da_m}{da_{total}} \cdot \frac{dU_m}{da_m} + \frac{da_f}{da_{total}} \cdot \frac{dU_f}{da_f} + \frac{da_i}{da_{total}} \cdot \frac{dU_i}{da_i}\right) \quad (10)$$

where B is the width of the crack. Applying Eq. (9) into differentiations of each member in Eq. (10) yields

$$SE_{\mathrm{IC}} = \frac{da_m}{da_{total}} G_{\mathrm{IC,m}} + \frac{da_f}{da_{total}} G_{\mathrm{IC,f}} + \frac{da_i}{da_{total}} G_{\mathrm{IC,i}} \quad (11)$$

For convenience of explanation, this equation is transformed

$$SE_{\mathrm{IC}} = \frac{\Delta a_m}{\Delta a_{total}} G_{\mathrm{IC,m}} + \frac{\Delta a_f}{\Delta a_{total}} G_{\mathrm{IC,f}} + \frac{\Delta a_i}{\Delta a_{total}} G_{\mathrm{IC,i}} \quad (12)$$

where Δa presents the propagated crack length of each region.

Considering the fiber debonding shown in Figure 7(a), $G_{\mathrm{IC,i}}$ is apparently small because of the weak interfacial strength between BF and PP, which is also indicated by other reports [10,30]. Besides, it is also reported that the interfacial debonding energy of glass fiber reinforced polypropylene, which has similar chemical composition to that of BF/PP, is 0.045 kJ/m^2 [32]. Thereby, the third member of Eq. (12) is negligibly small because its coefficient is less than 1 according to Eq. (7). Therefore, the interfacial debonding energy seems to have small influence on SE_{IC}.

On the other hand, $G_{\mathrm{IC,m}}$ seems to have large influence on SE_{IC} because of many multiple matrix cracks confirmed in Figure 8(b). However, the coefficient of the first member of Eq. (12) is less than 1. Accordingly, it is possible that SE_{IC} is less than G_{IC} of PP. Meanwhile, as confirmed in Figure 4, a little amount of fiber bridging was found. The fiber bridging energy of glass fiber reinforced

polypropylene with close fiber diameter to that of the specimen used in this study was reported 6.9 kJ/m^2 [33]. Therefore, it is also possible that SE_{IC} exceeds G_{IC} of PP affected by the amount of fiber bridging, while its average value can reach the close level of G_{IC} of PP. Consequently, we conclude that the measured SE_{IC} is an effective parameter for the separation criterion of BFPP unidirectional rods.

The representative fracture energy evaluating method of BF/PP rods proposed in this study can be also applied to any other combinations of composite rods. In addition, the parameter is essential to cohesive zone model analysis. Once the stress-strain relation of transverse direction, or separation-law, obtained, more precise predictions of deformation behaviour and residual strength under mode I stress condition of macro scale composites reinforced with composite rods can be expected.

4. Conclusion

This study proposed a new mode I-governed representative critical fracture energy called separation energy SE_{IC} for unidirectional BFPP rods using a modified double cantilever beam (DCB) test. We assert that the proposed approach can effectively measure SE_{IC} of BFPP rods and was evaluated at 1.5 ± 0.5 kJ/m^2. Some key points are summarized below:

- The linear relation between apparent crack length and cube root of compliance was identified, having a slope parallel to that of predictions using elastic beam theory.

- The average value of SE_{IC} was 1.5 ± 0.5 kJ/m^2 regardless of the apparent crack length.
- SEM observation of fracture surfaces revealed the interfacial debonding between BF and PP, matrix crack growth and fiber bridging.

Declaration of competing interest

The authors declare that they have no known competing financial interests or personal relationships that could have appeared to influence the work reported in this paper.

Acknowledgements

This research was promoted by COI program "Construction of next-generation infrastructure using innovative materials ~Realization of safe and secure society that can coexist with the Earth for centuries~ supported by Japan Science and Technology Agency (JST) Grant Number JPMJCE1315.

CRediT author contribution statement

Yuta Tobata: Conceptualization, Data curation, Formal analysis, Investigation, Methodology, Validation, Visualization; Roles/Writing - original draft, Writing - review & Editing.
Kimiyoshi Naito: Conceptualization, Data curation, Project administration, Resources, Supervision, Validation, Visualization, Writing - review & editing.
Jonathon David Tanks: Conceptualization, Methodology, Validation, Visualization, Writing - review &editing.

Reference

[1] Chen L, Steel-free bridge decks reinforced with FRP composites. In: Jain R, Lee L, editors. Fiber reinforced polymer (FRP) composites for infrastructure applications focusing on innovation, technology implementation and sustainability, Springer, New York: 2012. p.143-162.
[2] Liu Y, Zwingmann B, Schlaich M. Carbon fiber reinforced polymer for cable Structures—A Review. Polymers. 2015;7(10):2078-2099.
[3] Mayandi K, Rajini N, Ayrilmis N, Indira MPD, Siengchin S, Mohammad F, Al-Lohedan HA, An overview of endurance and ageing performance under various environmental conditions of hybrid polymer. J. Mater. Res. Technol. 2020;9(6):15962-15988.
[4] Dhand V, Mittal G, Rhee KY, Park S, Hui D, A short review on basalt fiber reinforced polymer composites. Compos Part B, 2015;73:166-180.
[5] Ahmed A, Guo S, Zhang Z, Shi C, Zhu D, A review on durability of fiber reinforced polymer (FRP) bars reinforced seawater sea sand concrete. Const Build Mater. 2020;256119484.

[6] Shubhra QTH, Alam A, Quaiyyum M, Mechanical properties of polypropylene composites: A review. J. Thermoplast. Compos. Mater. 2014;26(3)362-391.
[7] Maddah HA, Polypropylene as a promising plastic: A Review. Am J Polymer Sci 2016; 6(1):1-11.
[8] Tanks J, Naito K, Ueda H, Characterization of the static, creep, and fatigue tensile behavior of basalt fiber/polypropylene composite rods for passive concrete reinforcement. Polymers, 2021; 13: 3136.
[9] Botev M, Betchev H, Bikiaris D, Panayiotou C, Mechanical properties and viscoelastic behavior of basalt fiber-reinforced polypropylene. J. Appl. Polym. Sci. 1999;74:523-531.
[10] Czigany T, Special manufacturing and characteristics of basalt fiber reinforced hybrid polypropylene composites: Mechanical properties and acoustic emission study. Compos Sci Technol, 2006;66:3210-3220.
[11] Sang L, Zheng G, Hou W, Yang X, Wei Z, Crystallization and mechanical properties of basalt fiber-reinforced polypropylene composites with different elastomers. J. Therm. Anal. Calorim. 2018;134:1531-1543.
[12] Tang C, Xu FX, Li G, Combustion performance and thermal stability of basalt fiber-reinforced polypropylene composites. Polymers, 2019;11:1826.
[13] Russo P, Simeoli G, Climino F, Papa I, Ricciardi MR, Lopresto V, Impact damage behavior of vinyl ester-, epoxy-, and nylon 6-based basalt fiber composites. J. Mater. Eng. Perform 2019;28(6):3256-3266.
[14] Fu H, Feng X, Liu J, Yang Z, He C, Li S, An investigation on anti-impact and penetration performance of basalt fiber composites with different weave and lay-up modes, Def. Technol. 2020;16:787-801.
[15] Czigany T, Vad J, Poloskei K, Basalt fiber as a reinforcement of polymer composites. Period. Polytech., Mech. eng. 2005;49(1):3-14.
[16] Carlsson LA, Adams DF, Pipes RB, Characterization of Delamination Failure, Experimental characterization of advanced composite materials fourth edition, CRC Press, New York: 2014. p.250-257.
[17] Williams JG, The fracture mechanics of delamination tests, J Strain Anal Eng Des, 1989;24(4): 207-214
[18] Colombo C, Vergani L, Burman M, Static and fatigue characterization of new basalt fiber reinforced composites. Compos. Struct. 2012;94(3):1165-1174.
[19] Chen T, Harvey CM., Wang S, Silberschmidt VV., Analytical corrections for double-cantilever beam tests. Int J Fract 2021;229:269-276.
[20] Jones R, Kinloch A. J, Michopoulos JG, Brunner AJ, Phan N, Chapter Thirteen – Delamination growth in polymer – Matrix fibre composites and the use of fracture-mechanics data for material characterization and life predictions, Aircraft sustainment and repair, Butterworth-Heinemann, Oxford: 2018.p. 763-797

[21] Borg R, Nilsson L, Simonsson K, Simulating DCB, ENF and MMB experiments using shell elements and a cohesive zone model. Compos Sci Technol 2004;64:269-278.
[22] Østergaard RC, Sørensen BF, Interface crack in sandwich specimen. Int J Fract, 2007;143:301–316.
[23] Morais AB, Mode I cohesive zone model for delamination in composite beams. Eng Fract Mech 2013;109:235-245.
[24] Riano L, Belec L, Chailan JF, Joliff Y, Effect of interphase region on the elastic behaviour of unidirectional glass fber/epoxy composites. Compos Struct 2018;198:109-116.
[25] Chevalier J, Camanho PP, Lani F, Pardoen T, Multi-scale characterization and modelling of the transverse compression response of unidirectional carbon fiber reinforced epoxy. Compos Struct; 2019;209:160-176
[26] Mottram JT, Shear modulus of standard pultruded FRP material. J. Compos. Constr. 2004;8(2):1090-0268
[27] Gross B, Srawley JE, Stress intensity factors for single edge notch tension specimens by boundary collocation of a stress function. NASA TN D 2395, 1964.
[28] Tada H, Paris PC, Irwin GR, Stress analysis results for common test specimen configurations, The stress analysis of cracks handbook, 3rd ed, ASME Press, New York: 2000, p.52-54
[29] Kumar N, Gaur KK, Shakher C, Measurement of material constants (Young's modulus and Poisson's ratio) of polypropylene using digital speckle pattern interferometry (DSPI). J. JSEM. 2015;15:87-91.
[30] Botev M, Betchev H, Bikiaris D, Panayiotou C, Mechanical properties and viscoelastic behavior of basalt fiber reinforced polypropylene. J. Appl. Polym. Sci. 1999;74(3):523-531
[31] Desai KC, Kumar AS, Basu S, Parameswaran V, Measurement of cohesive parameters of crazes in polystyrene films, Exp. Appl Mech 2011;6:519-526.
[32] Copponnex TJ, Analysis and evaluation of the single fibre fragmentation test. Compos Sci Technol. 1996;56:893-909.
[33] Fu SY, Lauke B, the fibre pull-out energy of misaligned short fibre composites. J Mater Sci. 1997;32:1985-1993.

(a)

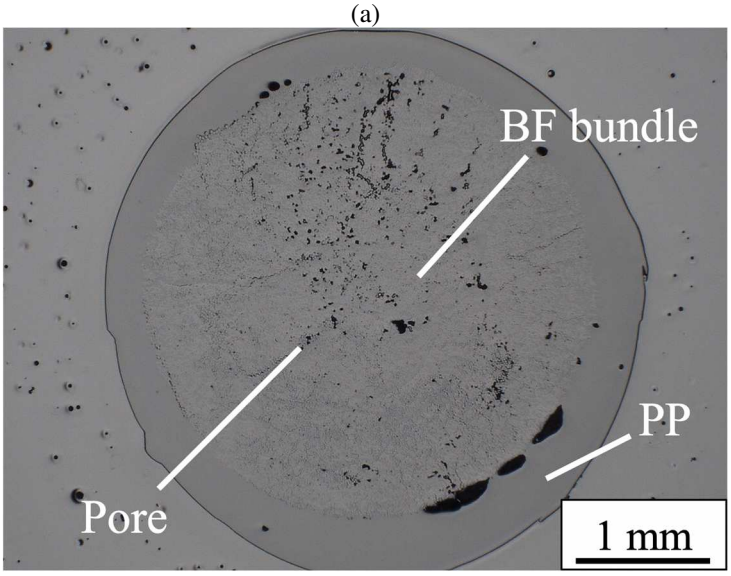

(b)

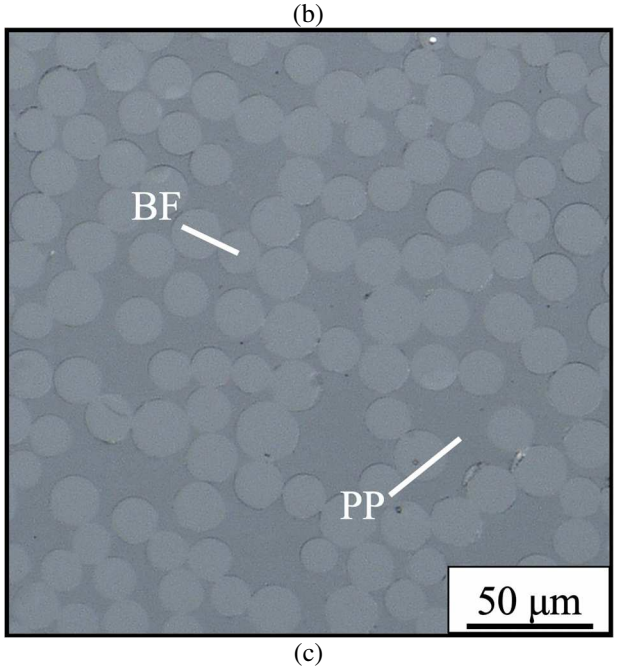

(c)

Figure 1. Digital micro scope image of BFPP rod structure (a) Surface image (b) Cross-section image (c) Magnified cross-section image

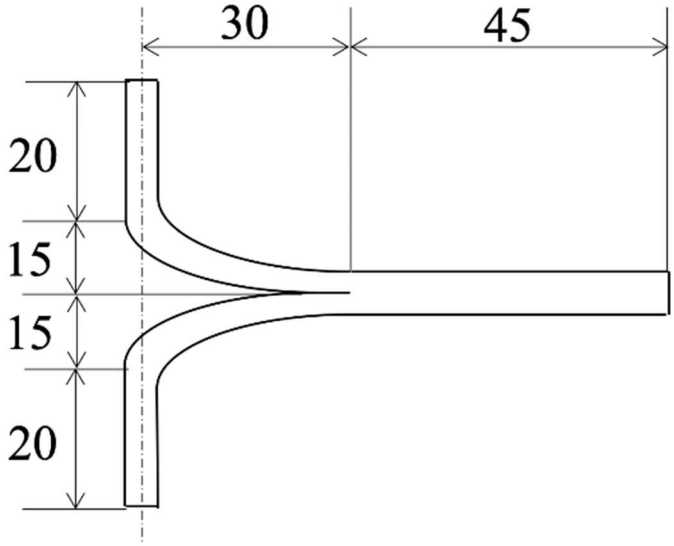

Figure 2. Dimensions of the DCB specimen

Figure 3. Configuration of the DCB test

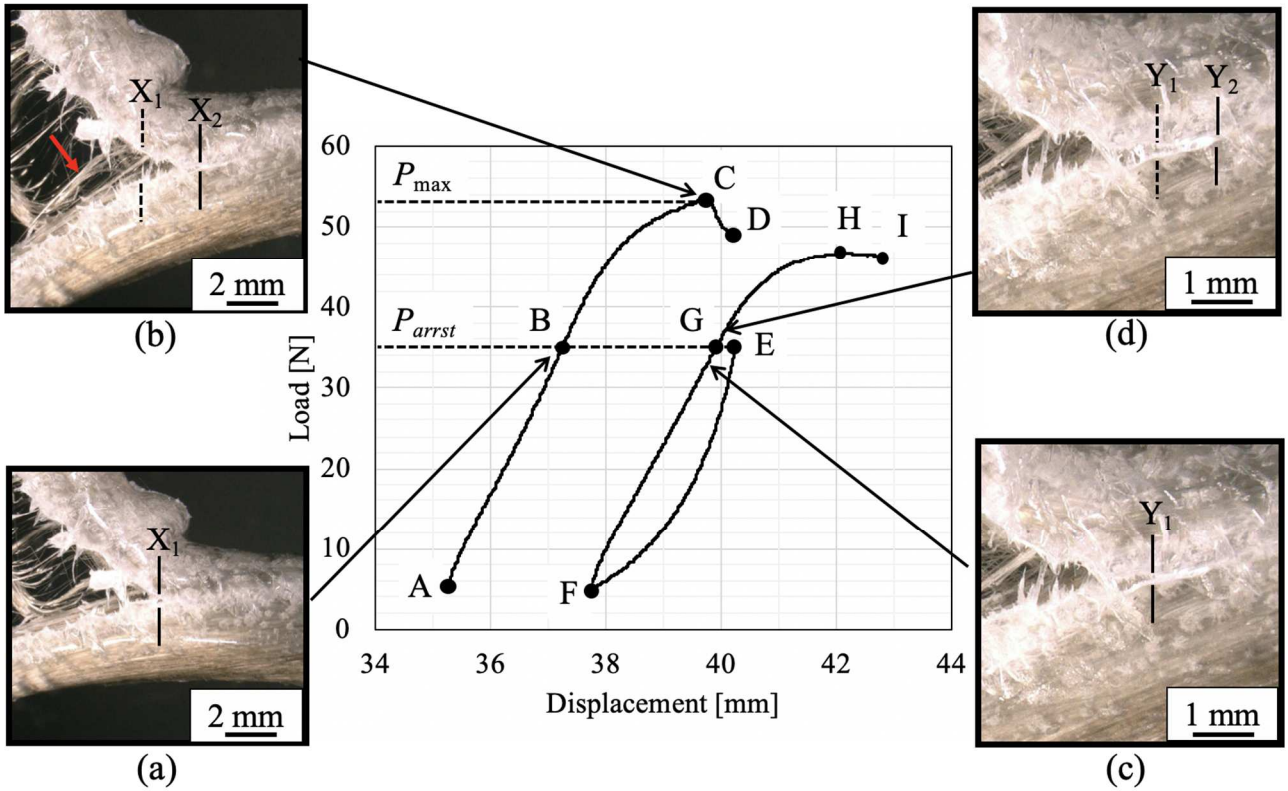

Figure 4. Typical loading-displacement curve. A-B: linear load-displacement relation section. C and H are the points of maximum load (P_{max}) of each cycle. D and I are the point of maximum displacement of each cycle. E is the end of cross head hold. F is the end of unloading. G is the point where its load is identical to that of E (P_{arrst}). Figure (a) and (b) present deformation behavior during point B and C. The arrow shows the bridging fiber. The lines X_1 and X_2 show the crack tip at B and C respectively. Figure (c) and (d) depict deformation behavior before and after P_{arrst} loaded around point G. The lines Y_1 and Y_2 show the crack tip at before and after reaching P_{arrst} respectively.

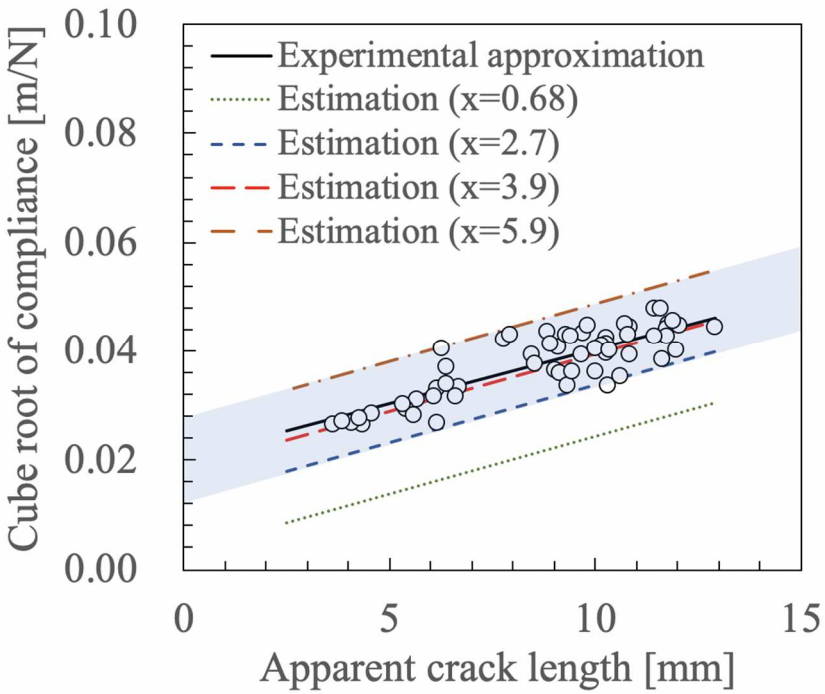

Figure 5. Relation between the apparent crack length and cube root of compliance. Solid line shows the experimental approximation. Broken lines present the estimation from the elastic beam theory as a function of x [16].

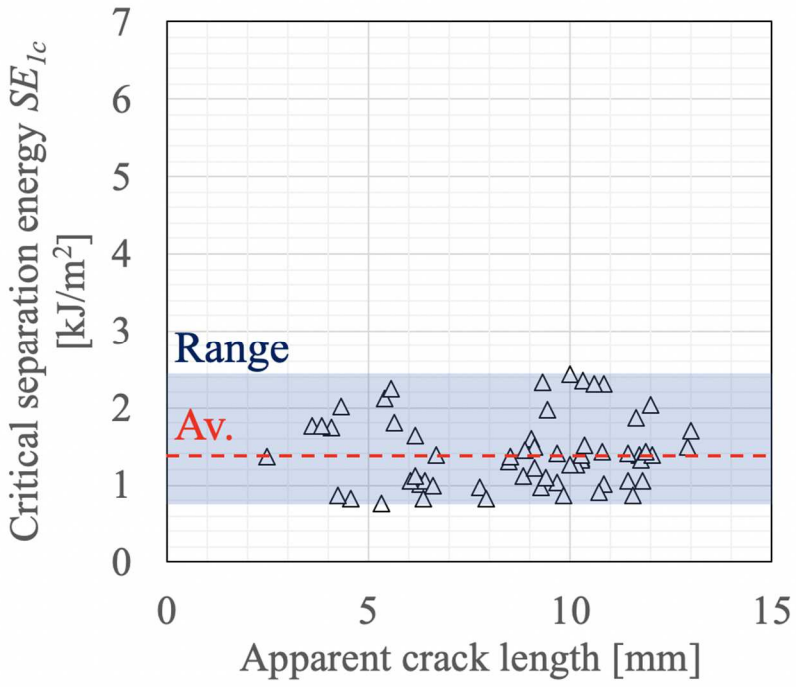

Figure 6. Relation between the apparent crack length and separation energy SE_{IC}

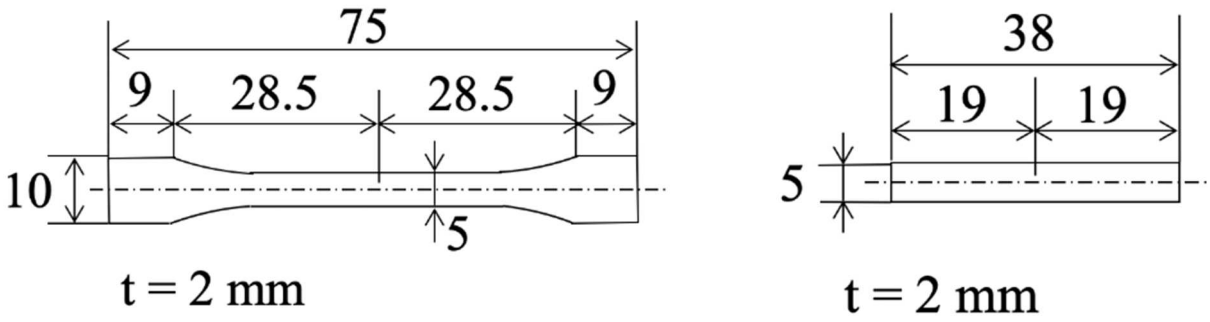

(**a**) (**b**)

Figure 7. The geometry of single edge notch test specimen (a) SENT (b) SENB. The notch size was cut into 1.5-1.8 mm length.

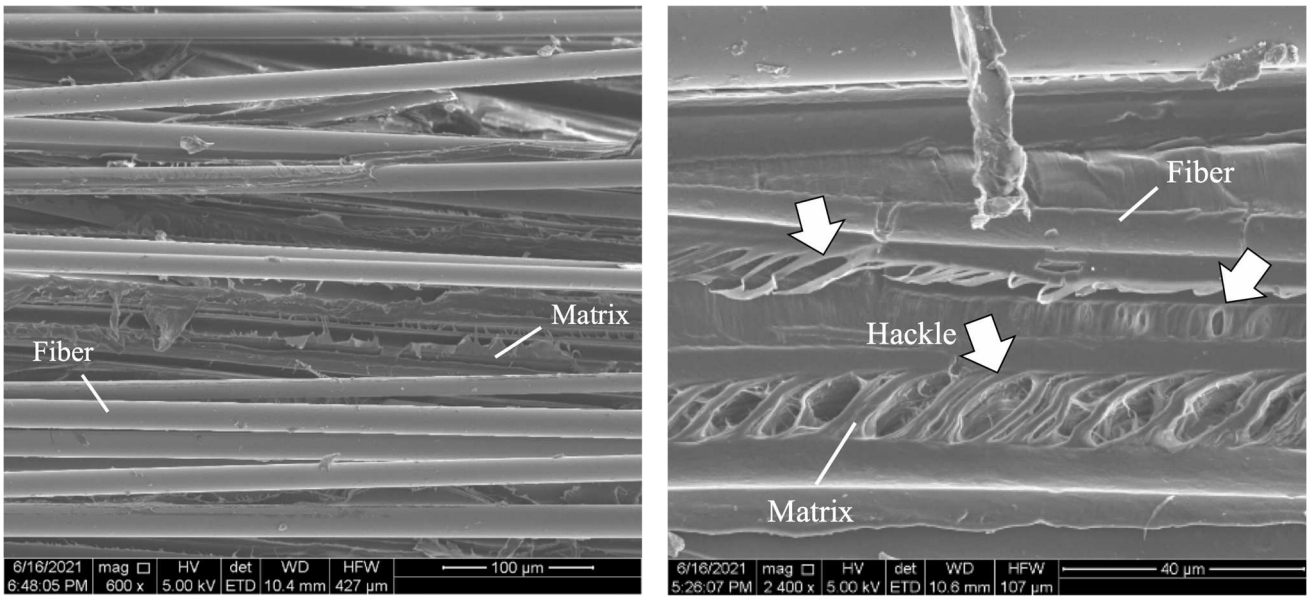

(**a**) (**b**)

Figure 8. SEM fracture surface image of a torn semi cylinder beam. (a) Typical example of fracture image (b) Matrix crack indicated with arrows.

Table 1 Summary of substitutions for K_{IC} and G_{IC} of PP, and SE_{IC} of BFPP rod

Poisson's ratio [24] [-]	Young's modulus [GPa]	K_{IC} [MPa·m$^{1/2}$]	G_{IC} [kJ/m^2]	SE_{IC} [kJ/m^2]
0.43	1.3 ± 0.1	1.5 (SENT) ±0.2 1.3 (SENB) ±0.1	1.4 (SENT) ±0.3 1.1 (SENB) ±0.2	1.5 ± 0.5